Probing the weakly-bound neutron orbit of ^{31}Ne with total reaction and one-neutron removal cross sections

W. Horiuchi,[1,*] Y. Suzuki,[2,†] P. Capel,[3,4,‡] and D. Baye[3,§]

[1]*Graduate School of Science and Technology, Niigata University, Niigata 950-2181, Japan*

[2]*Department of Physics, Faculty of Science and Graduate School of Science and Technology, Niigata University, Niigata 950-2181, Japan*

[3]*Physique Quantique, C.P. 165/82 and Physique Nucléaire Théorique et Physique Mathématique, C.P. 229, Université Libre de Bruxelles, B-1050 Brussels, Belgium*

[4]*National Superconducting Cyclotron Laboratory, Michigan State University, East Lansing, Michigan 48824, USA*

A candidate of a neutron-halo nucleus, ^{31}Ne, contains a single neutron in the pf shell. Within the Glauber and eikonal models, we analyze reactions used to study ^{31}Ne. We show in a ^{30}Ne $+ n$ model that the magnitudes of the total reaction and above all of the one-neutron removal cross sections of ^{31}Ne on ^{12}C and ^{208}Pb targets strongly depend on the orbital angular momentum of the neutron, thereby providing us with efficient ways to determine both the spin-parity and structure of the ground state of ^{31}Ne. Besides these inclusive observables, we also calculate energy and parallel-momentum distributions for the breakup of ^{31}Ne and show their strong dependence on the orbital of the valence neutron in the bound state of ^{31}Ne.

PACS number(s): 21.10.Gv, 21.10.Pc, 25.60.−t, 27.30.+t

I. INTRODUCTION

Exploring nuclei near the neutron and proton driplines is making rapid progress in and beyond the p- and sd-shell regions. The Ne isotopes raise interesting structure problems. The α cluster structure around ^{20}Ne has been known for many years [1,2]. Recently ^{17}Ne, an ^{15}O $+ p + p$ Borromean system, has been found to have a large charge radius due to a significant amount of s^2 component [3]. For the very neutron-rich Ne, Na, and Mg isotopes with $N \approx 20$, one of the most important issues is the vanishing of the shell gap, which causes a mixing of normal and intruder configurations and has significant influence on the properties of those nuclei [4–10]. The importance of deformation around ^{30}Ne is stressed in Refs. [7,8], in contrast to the result of a mean-field calculation [11]. The heaviest Ne isotope synthesized so far is ^{34}Ne. It may be a dripline nucleus considering that ^{33}Ne is unstable to neutron decay [12].

The nucleus ^{31}Ne with $N = 21$ neutrons attracts our special attention in view of its possible halo structure containing a $1p_{3/2}$ and/or $0f_{7/2}$ valence neutron. Its neutron separation energy S_n is 0.33 MeV, though it has large uncertainty [13]. The ground-state spin-parity of ^{31}Ne is thus expected to be either $3/2^-$ or $7/2^-$. The former possibility may happen because the single-particle energy of the neutron orbit with low orbital angular momentum receives a considerable shift near the neutron dripline [14,15]. Two calculations, one within a shell model [4] and one using a microscopic cluster model of ^{30}Ne $+ n$ [16], predict that shell inversion.

The rare isotope ^{31}Ne was first produced in a projectile fragmentation reaction [17]. Nowadays, an intense beam provided by the Radioactive Ion Beam Factory (RIBF) at RIKEN can produce ^{31}Ne in sufficiently large amounts (several particles per second). Very recently, the total reaction cross sections σ_R of heavy Ne isotopes on ^{12}C target [18] and the one-neutron removal cross sections σ_{-n} of ^{31}Ne on ^{12}C and ^{208}Pb targets have been measured for the first time around 230 MeV/nucleon [19]. The purpose of this article is to analyze the sensitivity of σ_R, σ_{-n} and other dissociation cross sections to the orbit of the ^{31}Ne valence neutron. During the completion of this theoretical work, the one-neutron removal cross sections of ^{31}Ne measured at RIKEN became available [19]. We seize this opportunity to compare our calculations with the data to draw conclusions about the structure of the ground state of ^{31}Ne.

We describe ^{31}Ne as a system consisting of a ^{30}Ne core (c) and a weakly bound valence neutron (n). The core is assumed to be in its 0^+ ground state though its excitation energy is fairly low. Considering that structure model we evaluate the total reaction and one-neutron removal cross sections within the Glauber formalism [20–23] on both light (^{12}C) and heavy (^{208}Pb) targets and compare the values obtained for the $1p_{3/2}$ and $0f_{7/2}$ possible configurations of the ^{31}Ne ground state. To predict the sensitivity of more exclusive observables (e.g., energy and parallel-momentum distributions) to the ground-state configuration, we also perform calculations within the eikonal model [20–22,24]. Since both light and heavy targets are considered, we use the Coulomb correction to the eikonal model (CCE) [25–27].

This article is structured as follows: After a summary of the Glauber and eikonal formalisms (Sec. II), we detail the inputs of our calculations in Sec. III. Our results and analysis are presented in Secs. IV and V. Section VI contains the conclusions and perspectives of this study.

II. THEORETICAL FRAMEWORK

As mentioned in the Introduction, we consider in this study two reaction models. First, the Glauber model [20–23] is used

─────────

*horiuchi@nt.sc.niigata-u.ac.jp

†suzuki@nt.sc.niigata-u.ac.jp

‡pierre.capel@centraliens.net

§dbaye@ulb.ac.be

to evaluate the total reaction and one-neutron removal cross sections of ^{31}Ne. Second, the eikonal model [20–22,24] is used to compute the dissociation cross section as a function of the energy and parallel-momentum between the ^{30}Ne core and the neutron after breakup [28,29]. Both models are based on Glauber's idea [24] to describe the influence of the collision onto the initial projectile-target wave function by a multiplying amplitude $e^{i\chi}$,

$$\Psi_f = e^{i\chi(\boldsymbol{b})}\Psi_i, \tag{1}$$

where the phase χ is assumed to depend only on the transverse component $\boldsymbol{b}$ of the projectile-target relative coordinate. In the present work, this phase is obtained by folding a profile function that describes nucleon-nucleon effective interactions with the projectile and target densities. In the eikonal approximation, however, it is more usual to derive it from optical potentials that simulate the interaction between the projectile constituents and the target.

In a general interpretation of the eikonal model [20], the adiabatic approximation employed in the Glauber model is not assumed, which invalidates the simple ansatz (1) [30]. The adiabatic approximation ignores the excitation energy compared to the incident energy, leading to a well-known unphysical result for the Coulomb dissociation. In order to solve this problem and still maintain Eq. (1), we only need to correct the Coulomb phase appropriately [25,26]. This approximate version is the CCE and its accuracy has been tested by comparison to the exact eikonal calculation in Ref. [27].

In this section, we briefly present both approaches, emphasizing their common points and differences that make them complementary.

A. Glauber formalism

Provided that ^{31}Ne can be seen as a neutron loosely bound to a ^{30}Ne core whose wave function is the same as that of an isolated ^{30}Ne, σ_{-n} can be obtained from the difference between the projectile and the core interaction cross sections [20,31,32]

$$\sigma_{-n}(^{31}\mathrm{Ne}) = \sigma_I(^{31}\mathrm{Ne}) - \sigma_I(^{30}\mathrm{Ne}). \tag{2}$$

Computing the interaction cross sections is not easy because it excludes inelastic scattering, which cannot be properly treated if no description of the internal structure of the projectile is considered. Fortunately, if the number of bound excited states is small, σ_I can be well approximated by the reaction cross section σ_R, which can be easily computed within the Glauber formalism [20,21,23]. For ^{31}Ne, which has only one known bound state, i.e., its ground state, this approximation is legitimate. For ^{30}Ne, however, $\sigma_R(^{30}\mathrm{Ne})$ will overestimate $\sigma_I(^{30}\mathrm{Ne})$ by $\sigma_{\mathrm{inel}}(^{30}\mathrm{Ne})$, in which the projectile is excited toward its 2^+ and 4^+ bound excited states. Nevertheless, the inelastic scattering being a phenomenon occurring near the nuclear surface, its contribution is not expected to be significant at incident energies of 200–300 MeV/nucleon where the surface transparency becomes large. The approximation

$$\sigma_{-n}(^{31}\mathrm{Ne}) \approx \sigma_R(^{31}\mathrm{Ne}) - \sigma_R(^{30}\mathrm{Ne}) \tag{3}$$

seems thus reasonable.

The Glauber model expresses the nuclear part of the reaction cross section for a nucleus X impinging on a target T as the integral of the reaction probability with respect to the transverse components $\boldsymbol{b}$ of the X-T relative coordinate [20,21,23]

$$\sigma_R = \int (1 - |e^{i\chi(\boldsymbol{b})}|^2)d\boldsymbol{b}, \tag{4}$$

where the phase-shift function χ models the nuclear interactions between the colliding nuclei. As mentioned earlier, in the Glauber formalism, this phase is expressed as a function of the densities of the target ρ_T and the impinging nucleus ρ_X. It also depends on profile functions Γ_{NN} describing effective nuclear interactions between the nucleons. At the optical limit approximation of the Glauber model (OLA) the nuclear phase-shift functions are usually given by [20,21,23]

$$\chi^N(\boldsymbol{b}) = i \iint \rho_T(\boldsymbol{r}')\rho_X(\boldsymbol{r}'')\Gamma_{NN}(\boldsymbol{b} - \boldsymbol{s}' + \boldsymbol{s}'')d\boldsymbol{r}''d\boldsymbol{r}', \tag{5}$$

where $\boldsymbol{s}'$ and $\boldsymbol{s}''$ are the transverse components of the internal coordinate of the target ($\boldsymbol{r}'$) and the impinging nucleus ($\boldsymbol{r}''$), respectively. The OLA is therefore equivalent to the double-folding of an effective nucleon-nucleon interaction. Note that the profile functions Γ_{NN} depend on the nucleons considered: Their expression for identical nucleons (pp or nn) is not the same as for the proton-neutron (pn) interaction. Therefore, in our calculations, expression (5) is actually split into four terms. This is done as follows: Replace $\rho_X \Gamma_{NN}$ with $\rho_X^p \Gamma_{Np} + \rho_X^n \Gamma_{Nn}$ using the proton and neutron densities of the projectile X and change ρ_T by $\rho_T^p + \rho_T^n$ followed by renaming N of Γ_{NN} in accordance with the density.

As shown by Abu-Ibrahim and Suzuki, the OLA (5) misses some higher-order terms, which can be included using the symmetrized expression [33,34]

$$\chi^N(\boldsymbol{b}) = \frac{i}{2}\left(\int d\boldsymbol{r}'\rho_T(\boldsymbol{r}')\left\{ 1 - \exp\left[-\int d\boldsymbol{r}''\rho_X(\boldsymbol{r}'') \right.\right.\right.$$
$$\left.\left. \times \Gamma_{NN}(\boldsymbol{b} + \boldsymbol{s}' - \boldsymbol{s}'') \right] \right\}$$
$$+ \int d\boldsymbol{r}''\rho_X(\boldsymbol{r}'')\left\{ 1 - \exp\left[-\int d\boldsymbol{r}'\rho_T(\boldsymbol{r}') \right.\right.$$
$$\left.\left.\left. \times \Gamma_{NN}(\boldsymbol{b} - \boldsymbol{s}' + \boldsymbol{s}'') \right] \right\} \right). \tag{6}$$

The Glauber calculations presented in the following are performed using this expression (6) in Eq. (4). Again the actual phase-shift function in our calculations is split into four terms. The details about the calculation of the densities and the profile functions are summarized in Sec. III.

For the carbon target, the Coulomb contribution to the total reaction cross section is neglected, the reaction being fully nuclear dominated. However, this may no longer be done for heavy targets. For the lead target, we add incoherently to the nuclear reaction cross section (4) the Coulomb contribution at first-order (see Sec. IV B).
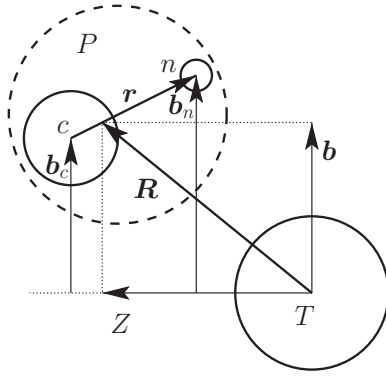
FIG. 1. Jacobi set of coordinates used for the eikonal calculations: $\boldsymbol{r}$ is the projectile internal coordinate, and $\boldsymbol{r} = \boldsymbol{b} + Z\widehat{\boldsymbol{Z}}$ is the target-projectile coordinate. The transverse components of the core-target and neutron-target coordinates are denoted by $\boldsymbol{b}_c$ and $\boldsymbol{b}_n$, respectively.

B. Coulomb-corrected eikonal description of reactions

Since we are also interested in the influence of the ^{31}Ne structure on other observables, like energy and parallel-momentum distributions, we perform calculations within the eikonal model [20,21,24]. Indeed this model enables us to compute differential cross sections considering both Coulomb and nuclear interactions as well as their interferences [28,29]. The eikonal model assumes a cluster structure of the projectile and usually describes the interaction between the clusters and the target by optical potentials.

In this work, the projectile P (^{31}Ne) is assumed to be made up of a neutron n of mass m_n initially bound to a ^{30}Ne core c of mass m_c and charge $Z_c e$. This two-body projectile is impinging on a target T of mass m_T and charge $Z_T e$. The neutron has spin $I = 1/2$, while both core and target are assumed to be of spin zero. These three bodies are seen as structureless particles. Figure 1 schematizes the set of coordinates we use in the following. The c-n relative coordinate is denoted by $\boldsymbol{r}$ and the P-T relative coordinate by $\boldsymbol{r}$, with Z and $\boldsymbol{b}$ its longitudinal and transverse components, respectively. In Fig. 1, the transverse parts of the c-T ($\boldsymbol{b}_c$) and n-T ($\boldsymbol{b}_n$) coordinates are shown as well.

The structure of the projectile is described by the internal Hamiltonian

$$H_0 = \frac{p^2}{2\mu_{cn}} + V_{cn}(\boldsymbol{r}), \tag{7}$$

where $\boldsymbol{p}$ is the relative momentum of the neutron to the core, $\mu_{cn} = m_c m_n / m_P$ is the reduced mass of the core-neutron pair (with $m_P = m_c + m_n$), and V_{cn} is the potential describing the core-neutron interaction. This potential includes a central part, and a spin-orbit coupling term (see Sec. III).

In partial wave lj, the eigenstates of H_0 are defined by

$$H_0 \phi_{ljm}(E, \boldsymbol{r}) = E \phi_{ljm}(E, \boldsymbol{r}), \tag{8}$$

where E is the energy of the c-n relative motion and j is the total angular momentum resulting from the coupling of the orbital momentum l with the neutron spin I. The negative-energy solutions of Eq. (8) correspond either to the physical bound state of the projectile or to orbitals occupied by the neutrons of the core, which are forbidden to the valence

neutron by the Pauli principle. The former is denoted by $\phi_{l_0 j_0 m_0}(E_0)$ in the following. These wave functions are normed to unity. The positive-energy states describe the broken-up projectile. Their radial part $r^{-1} u_{klj}$ are normalized according to

$$u_{klj}(r) \xrightarrow[r \to \infty]{} \cos \delta_{lj} F_l(kr) + \sin \delta_{lj} G_l(kr), \tag{9}$$

where $k = \sqrt{2\mu_{cn} E / \hbar^2}$ is the wave number, δ_{lj} is the phase shift at energy E, and F_l and G_l are respectively the regular and irregular Coulomb functions [35].

At the eikonal approximation, the amplitude appearing in Eq. (1) can be divided into three factors [27]

$$e^{i\chi} = e^{i\chi_{PT}^C} e^{i\chi^C} e^{i\chi^N}, \tag{10}$$

where the dependence on the transverse coordinate $\boldsymbol{b}$ has been omitted for clarity. The elastic Coulomb phase χ_{PT}^C describes the projectile-target Rutherford scattering. It reads [24]

$$\chi_{PT}^C(b) = 2\eta \ln(Kb), \tag{11}$$

where K is the wave number of the projectile-target relative motion and $\eta = Z_T Z_c e^2 / (4\pi \epsilon_0 \hbar v)$ is the P-T Sommerfeld parameter, with v the initial P-T relative velocity.

Besides the deflection of the projectile trajectory, the Coulomb interaction also contributes to the breakup of the projectile. Acting only on the core, it indeed induces a tidal force between both components of the projectile. The Coulomb phase χ^C in Eq. (10) simulates that tidal force (see, e.g., Eqs. (16) and (17) of Ref. [27]). The slow decrease of this phase at large b leads to divergence in the calculation of the breakup cross sections [27]. To overcome this problem, Margueron, Bonaccorso, and Brink have proposed a correction to this Coulomb term [25]. It consists in replacing at first order the Coulomb phase χ^C by the first order of the perturbation theory χ^{FO} (see Eq. (22) of Ref. [27]) following

$$e^{i\chi^C} \to e^{i\chi^C} - i\chi^C + i\chi^{FO}. \tag{12}$$

Because at large b the first-order phase χ^{FO} decays exponentially, correction (12) solves the aforementioned divergence problem. In addition, it restores most of the missing dynamical effects in the eikonal model, which enables us to describe reactions taking on (nearly) the same footing both Coulomb and nuclear interactions at all orders [27].

In the eikonal model, the nuclear interactions between the projectile constituents and the target are usually described by optical potentials chosen in the literature. In that case, the nuclear phase χ^N is expressed as integrals over Z of these potentials [20,21,24]. In the present case, no experimental data exist to constrain such a potential for the interaction between the ^{30}Ne core and the target. Following Ref. [23], we approximate the nuclear phase for each projectile constituent by the OLA (5). Therefore

$$\chi^N(\boldsymbol{b}, \boldsymbol{s}) = \chi_{cT}^N(\boldsymbol{b}_c) + \chi_{nT}^N(\boldsymbol{b}_n), \tag{13}$$

where χ_{cT}^N and χ_{nT}^N are respectively the c-T and n-T nuclear phases. They are computed using Eq. (5), in which the density ρ_X is replaced by the ^{30}Ne density or a Dirac delta function, respectively.

To evaluate elastic-breakup cross sections within the CCE we proceed as explained in Ref. [27]. The elastic-breakup amplitude reads

$$S_{kljm}^{(m_0)}(b) = e^{i(\sigma_l + \delta_{lj} - l\pi/2 + \chi_{PT}^C)} \langle \phi_{ljm}(E) |$$
$$\left(e^{i\chi^C} - i\chi^C + i\chi^{FO}\right) e^{i\chi^N} | \phi_{l_0 j_0 m_0}(E_0) \rangle, \quad (14)$$

where σ_l is the Coulomb phase shift [35].

In the following, we consider two breakup observables. The first is the breakup cross section as a function of the c-n relative energy E after dissociation

$$\frac{d\sigma_{bu}}{dE} = \frac{4\mu_{cn}}{\hbar^2 k} \frac{1}{2j_0 + 1} \sum_{m_0} \sum_{ljm} \int_0^\infty b\,db \left| S_{kljm}^{(m_0)}(b) \right|^2. \quad (15)$$

The second breakup observable is the parallel-momentum distribution

$$\frac{d\sigma_{bu}}{dk_\parallel} = \frac{8\pi}{2j_0 + 1} \sum_{m_0} \int_0^\infty b\,db \int_{|k_\parallel|}^\infty \frac{dk}{k} \sum_{\nu m}$$
$$\left| \sum_{lj} (lIm - \nu\nu|jm) Y_l^{m-\nu}(\theta_k, 0) S_{kljm}^{(m_0)}(b) \right|^2, \quad (16)$$

where $\theta_k = \arccos(k/k_\parallel)$ is the colatitude of the c-n relative wave vector $\boldsymbol{k}$ after breakup.

III. DENSITIES AND POTENTIALS

The calculation of the cross sections described in the previous section requires projectile and target densities and profile functions. In our study, we follow Ref. [23].

We first construct ^{30}Ne densities. We assume the internal wave function of this nucleus to be a Slater determinant of single-particle orbitals generated from the following potential

$$U(r) = -V_0 f(r) + V_1 r_0^2 \boldsymbol{l} \cdot \boldsymbol{s} \frac{1}{r} \frac{d}{dr} f(r) + V_C(r) \frac{1 - \tau_3}{2}, \quad (17)$$

where τ_3 has eigenvalue 1 for neutrons and -1 for protons, and f is the Woods-Saxon form factor

$$f(r) = \{1 + \exp[(r - R)/a]\}^{-1}, \quad (18)$$

where radius $R = r_0 A^{1/3}$ with $A = 30$. The spin-orbit strength is set to follow the systematics [36],

$$V_1 = 22 - 14[(N - Z)/A]\tau_3 \quad (19)$$

in MeV. The Coulomb potential V_C is taken from a uniform charge distribution. The values of r_0 and a are varied around standard values, and V_0 is determined separately for neutrons and protons to fit S_n and S_p. The resulting values are denoted V_0^n and V_0^p, respectively.

The neutron and proton densities of ^{30}Ne, ρ_c^n and ρ_c^p are calculated from the occupied orbits by removing approximately the effect of the center of mass motion [23]. The root-mean-square (rms) radii for neutron, proton, and matter distributions (r_c^n, r_c^p, r_c^m) are listed in Table I. The table also contains $\sigma_R(^{30}$Ne) for a ^{12}C target at 100, 240, and 1000 MeV/nucleon. The second value of the incident

TABLE I. Single-particle potentials for ^{30}Ne, rms radii of ^{30}Ne, and total reaction cross sections of ^{30}Ne + ^{12}C collision at the incident energies of 100, 240, and 1000 MeV/nucleon. Lengths, energies, and cross sections are given in units of fm, MeV, and b.

r_0	a	V_0^n	V_0^p	r_c^n	r_c^p	r_c^m	σ_R		
							100	240	1000
	0.65	43.71	72.53	3.36	2.58	3.12	1.54	1.29	1.38
1.20	0.70	43.81	73.55	3.40	2.59	3.16	1.56	1.31	1.39
	0.75	43.85	74.52	3.46	2.59	3.20	1.59	1.33	1.41
	0.65	41.01	68.83	3.44	2.74	3.22	1.58	1.33	1.41
1.25	0.70	41.15	69.79	3.48	2.73	3.25	1.60	1.34	1.43
	0.75	41.22	70.72	3.52	2.72	3.28	1.62	1.36	1.44

energy is chosen because it is close to that of the RIKEN experiment [18,19] and because profile functions are available at that energy [37]. The choice of Γ_{NN} is explained later in this section.

Since ^{31}Ne is assumed to exhibit a ^{30}Ne-n cluster structure, its densities are obtained from the ^{30}Ne densities computed above and the wave function ϕ_{ljm} for the ^{30}Ne-n relative motion. The latter is determined by solving the Schrödinger equation (8) in either the $1p_{3/2}$ or $0f_{7/2}$ orbital. The ^{30}Ne-n interaction is simulated by the same mean-field potential as for ^{30}Ne (17), but with a different central depth V_0.

Figure 2 displays the single-particle energies of $1p_{3/2}$ and $0f_{7/2}$, $\varepsilon(p)$ and $\varepsilon(f)$, as a function of V_0 for three choices of diffuseness parameter a, the radius parameter being fixed to $r_0 = 1.25$ fm. With increasing a, $\varepsilon(p)$ decreases very rapidly, whereas $\varepsilon(f)$ shows a mild change. It is therefore possible to obtain the expected shell inversion by considering a sufficiently large diffuseness (e.g., $a = 0.75$ fm). For actual calculations, the strength V_0 is set to reproduce the S_n value of 0.33 MeV (see Table II). Note that these potentials are also used as V_{cn} in the calculations of the wave functions ϕ_{ljm} that appear in the eikonal model (see Sec. II B).

The proton and neutron densities of ^{31}Ne, ρ_P^p, and ρ_P^n, are calculated including the recoil effect, which means that the difference between the centers of mass of ^{31}Ne and ^{30}Ne is treated properly

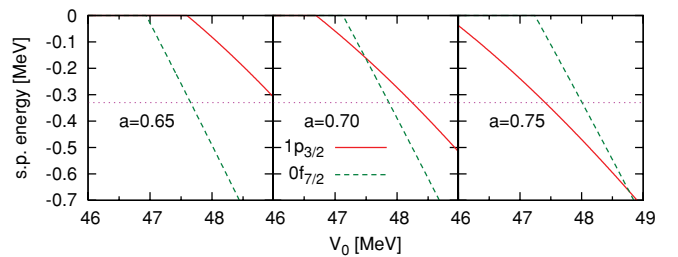$$\rho_P^p(\boldsymbol{r}') = \overline{\rho}_c^p(\boldsymbol{r}') \quad (20)$$

FIG. 2. (Color online) Single-particle energies of the $1p_{3/2}$ (full lines) and $0f_{7/2}$ (dashed lines) valence neutrons of ^{31}Ne as a function of V_0 for three different diffuseness parameters a (fm). The r_0 value is 1.25 fm. Horizontal dotted line at -0.33 MeV denotes the experimental energy.

TABLE II. Properties of the potentials describing ^{31}Ne. Using various potential geometries, we adjust $S_n = 0.33$ MeV in either the $1p_{3/2}$ orbit or the $0f_{7/2}$ one. Last-line potential reproduces $S_n = 0.60$ MeV in the $1p_{3/2}$ orbital. Rms radii of the corresponding densities are listed as well as the total reaction cross sections of ^{31}Ne+^{12}C at incident energies of 100, 240, and 1000 MeV/nucleon. Lengths, energies, and cross sections are given in units of fm, MeV, and b.

r_0	a	V_0	$\varepsilon(p)$	$\varepsilon(f)$	r_n	r_P^n	r_P^p	r_P^m	σ_R		
									100	240	1000
	0.65	52.28	-0.22	-0.33	4.25	3.40	2.59	3.16	1.58	1.32	1.41
1.20	0.70	51.82	-0.33	-0.05	7.20	3.66	2.60	3.35	1.70	1.41	1.50
	0.75	50.87	-0.33	–	7.35	3.72	2.60	3.40	1.72	1.43	1.52
	0.65	47.65	-0.01	-0.33	4.39	3.48	2.74	3.26	1.61	1.35	1.43
1.25	0.70	47.87	-0.24	-0.33	4.47	3.52	2.73	3.29	1.63	1.37	1.45
	0.75	47.41	-0.33	-0.07	7.44	3.79	2.73	3.48	1.75	1.45	1.55
1.25	0.75	48.52	-0.60	-0.55	6.62	3.71	2.73	3.43	1.74	1.44	1.54

$$\rho_P^n(\boldsymbol{r}') = \overline{\rho}_c^n(\boldsymbol{r}') + \rho_n(\boldsymbol{r}'), \qquad (21)$$

where $\boldsymbol{r}'$ is the internal coordinate of ^{31}Ne. In these expressions, $\overline{\rho}_c^p$ and $\overline{\rho}_c^n$ are the contributions of the ^{30}Ne core to the ^{31}Ne densities. They slightly differ from the densities of ^{30}Ne, because of the recoil effect

$$\overline{\rho}_c^{p/n}(\boldsymbol{r}') = \frac{1}{2j+1} \sum_m \int \rho_c^{p/n} \left(\frac{1}{A+1}\boldsymbol{r} + \boldsymbol{r}' \right) |\phi_{ljm}(\boldsymbol{r})|^2 d\boldsymbol{r}, \qquad (22)$$

where $\boldsymbol{r}$ is the ^{30}Ne-n relative coordinate. In Eq. (21) ρ_n denotes the contribution of the valence neutron to the ^{31}Ne density

$$\rho_n(\boldsymbol{r}') = \frac{1}{2j+1} \sum_m \int \delta \left(\frac{A}{A+1}\boldsymbol{r} - \boldsymbol{r}' \right) |\phi_{ljm}(\boldsymbol{r})|^2 d\boldsymbol{r}. \qquad (23)$$

Figure 3 displays the matter density of ^{31}Ne ($\rho_P = \rho_P^p + \rho_P^n$) as well as its contributions from the ^{30}Ne core ($\overline{\rho}_c = \overline{\rho}_c^p + \overline{\rho}_c^n$) and the valence neutron (ρ_n). The $1p_{3/2}$ orbit (left panel) reaches far in distances and extends the tail of the ^{30}Ne density significantly beyond 6 fm. On the contrary, the $0f_{7/2}$ orbit (right panel) changes the density only slightly even near the surface.
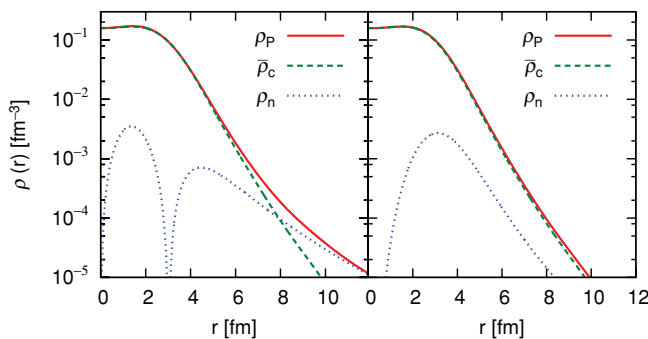

FIG. 3. (Color online) Matter density of ^{31}Ne (full lines) and contributions from the ^{30}Ne core (dashed lines) and the valence neutron (dotted lines). The r_0 value is 1.25 fm, and a is 0.75 fm for the $1p_{3/2}$ orbit (left panel) and 0.70 fm for the $0f_{7/2}$ orbit (right panel).

Table II lists the valence-neutron single-particle energies (ε); the rms radii of ^{31}Ne for the neutron, proton, and matter distributions (r_P^n, r_P^p, r_P^m); and $\sigma_R(^{31}$Ne) for a ^{12}C target at 100, 240, and 1000 MeV/nucleon. We also give the rms radius of the valence-neutron orbit $r_n = \sqrt{\langle \boldsymbol{r}^2 \rangle}$. This r_n value turns out to be around 7 fm for the $1p_{3/2}$ orbit but, due to the larger centrifugal barrier, is much smaller for the $0f_{7/2}$ orbit: about only 4 fm. Interestingly, although the matter radii of ^{31}Ne and ^{30}Ne depend on the potential sets (see Tables I and II), their difference remains unchanged: $\Delta r = r_P^m - r_c^m$ is 0.19–0.20 for $1p_{3/2}$ and 0.04 fm for $0f_{7/2}$. The constancy of Δr within the set of the same l suggests that Δr is insensitive to the shape of the potential but determined by S_n and l. Despite the fact that the single-particle energy is only -0.33 MeV, Δr is not very large even for $1p_{3/2}$ because the mass number of the core nucleus is fairly large.

Since the neutron separation energy S_n of ^{31}Ne is not accurately known, we also perform calculations with a slightly deeper potential (see last line of Table II) in order to examine the S_n dependence of $\sigma_R(^{31}$Ne) and $\sigma_{-n}(^{31}$Ne) values. This potential gives $\varepsilon(p) = -0.6$ MeV instead of -0.33 MeV. The matter radius is reduced by only 0.05 fm, but the r_n value changes by about 0.8 fm. The decrease of $\sigma_R(^{31}$Ne), and thus of $\sigma_{-n}(^{31}$Ne), on carbon is only about 10 mb. However, the $\sigma_{-n}(^{31}$Ne) value on lead is expected to be considerably reduced. We will discuss this in Sec. IV B.

The target densities used in our calculations are obtained from experimental data. For both ^{12}C and ^{208}Pb, the proton densities are derived from empirical charge densities by removing the finite size effect of protons. The neutron density of ^{12}C is obtained as explained in Ref. [23]. For ^{208}Pb, the neutron density is obtained by subtracting the proton density from the matter density [32] taken from a Hartree-Fock calculation.

Other key inputs to compute the cross sections of Sec. II are the profile functions Γ_{NN} that correspond to effective nucleon-nucleon interactions. These functions are parametrized in the usual way [23,37]

$$\Gamma_{NN}(\boldsymbol{b}) = \frac{1 - i\alpha_{NN}}{4\pi\beta_{NN}} \sigma_{NN}^{tot} \exp \left(-\frac{b^2}{2\beta_{NN}} \right), \qquad (24)$$

where σ_{NN}^{tot} is the total cross section for the NN collision, α_{NN} is the ratio of the real to the imaginary part of the NN-scattering amplitude, and β_{NN} is the slope parameter of the NN elastic differential cross section. The values of these parameters are taken from Ref. [37]. Note that they differ for the interaction between identical nucleons (pp or nn) and for the interaction between a proton and a neutron (pn). To analyze the sensitivity of our calculations to this choice of profile functions, we also perform calculations that ignore the difference between pp (or nn) and pn interactions. In those tests, we use the parameters of Γ_{NN} given in Ref. [23].

The profile functions (24) combined to the densities of ^{30,31}Ne and of the target enable us to compute the phase shifts (6) for the Glauber calculation. The same parameters are used to derive the OLA (5) used in the Coulomb-corrected eikonal calculation. To this end, the densities of the projectile and the target are expanded on a Gaussian basis

$$\rho(r) \approx \sum_i c_i \exp\left(-\frac{1}{2}a_i r^2\right). \quad (25)$$

This enables us to solve analytically the integrals appearing in Eq. (5) and partly in Eq. (6). The values c_i and a_i are available from the authors.

In the eikonal model, the nuclear phase (5) is added to the elastic Coulomb phase (11) and the corrected Coulomb phase (12) to obtain the eikonal phase (10). That phase is then numerically expanded into multipoles of rank λ. To this end, we use a Gauss quadrature on the unit sphere similar to the one considered to solve the time-dependent Schrödinger equation in Ref. [38]. The number of points along the colatitude is set to $N_\theta = 12$, and the number of points along the azimuthal angle is $N_\varphi = 30$ in most cases but goes up to 40 when large λs are considered. For the carbon target, the calculation requires a rather large number of multipoles: $\lambda_{max} = 16$ in the $1p_{3/2}$ case, and $\lambda_{max} = 12$ in the $0f_{7/2}$ one. For the lead target, a smaller number of multipoles is needed: $\lambda_{max} = 8$ for the $1p_{3/2}$ state and $\lambda_{max} = 6$ for the $0f_{7/2}$ one.

The eigenfunctions of the projectile Hamiltonian H_0 (8) are computed numerically with the Numerov method using 1000 radial points equally spaced from $r = 0$ up to $r = 100$ fm. This rather large value is required in order to reach convergence in the radial integrals appearing in Eq. (14) and in the calculation of r_n, the rms radius of the valence neutron (see Table II). The integrals over b appearing in Eqs. (15) and (16) are performed numerically from $b = 0$ up to $b = 400$ fm with a step $\Delta b = 1$ fm. In the $1p_{3/2}$ case this integral had to be done up to 600 fm to reach convergence when a lead target was considered.

IV. DISCUSSION OF THE $1p_{3/2}$ AND $0f_{7/2}$ ASSUMPTIONS WITHIN THE GLAUBER MODEL

A. Total reaction cross sections

Figure 4 compares $\sigma_R(^{31}\text{Ne})$ on a ^{12}C target calculated within the Glauber model (see Sec. II A) for the $1p_{3/2}$ (full line) and $0f_{7/2}$ (dashed line) orbits as a function of the ^{31}Ne incident energy. The phase-shift function is calculated using Eq. (6). The projectile density is obtained using the potential sets of radius $r_0 = 1.25$ fm with diffuseness $a = 0.75$ fm for the $1p_{3/2}$
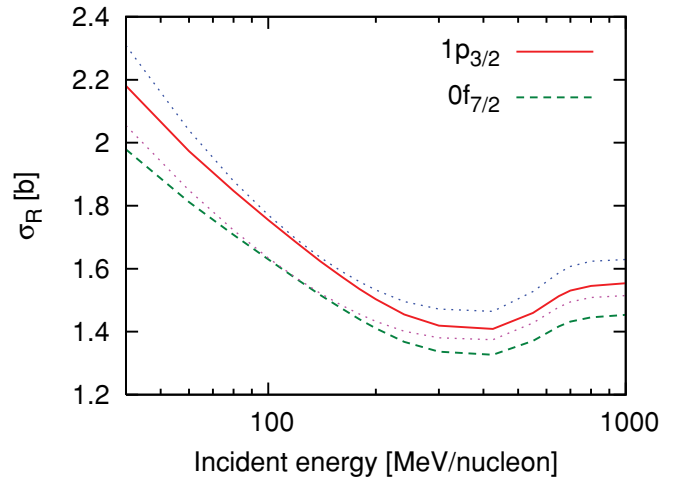
FIG. 4. (Color online) Total reaction cross section of ^{31}Ne on a ^{12}C target as a function of incident energy. Dotted lines are the results with the OLA phase shifts (5). See caption of Fig. 3 for r_0 and a.

orbit and $a = 0.70$ fm for the $0f_{7/2}$ orbit. At all energies the relative difference in σ_R between both configurations is about 5–10%. For example, as listed in Table II, $\sigma_R(^{31}\text{Ne})$ at 240 MeV/nucleon is 1.45 b for the p orbit and 1.37 b for the f one. Thus the difference of $\sigma_R(^{31}\text{Ne})$ depending on whether the orbital angular momentum of the valence neutron is 1 or 3 amounts to 87 mb. Though not very large, this difference may be sufficient to determine which assignment is favorable in comparison with experiment [18].

The reaction cross section is larger for a $1p_{3/2}$ neutron than for the $0f_{7/2}$ neutron because the integral appearing in the phase shifts (6) extends on a larger domain in the former case than in the latter. This variation in $\sigma_R(^{31}\text{Ne})$ with the projectile configuration, being mostly due to the change in the valence-neutron orbital is therefore rather small. Indeed, most of $\sigma_R(^{31}\text{Ne})$ is contributed by the ^{30}Ne core, whose reaction cross section does not vary much with the potential set: $\sigma_R(^{30}\text{Ne}) = 1.36$ b for $r_0 = 1.25$ fm and $a = 0.75$ fm and 1.34 b for $r_0 = 1.25$ fm and $a = 0.70$ fm. On the contrary, the increase in σ_R due to the addition of the valence neutron, $\sigma_R(^{31}\text{Ne}) - \sigma_R(^{30}\text{Ne})$, is strongly dependent on the assumed configuration: The increase turns out to be 96 mb for the $1p_{3/2}$ orbit and 26 mb for the $0f_{7/2}$ orbit at 240 MeV/nucleon. Following Eq. (3), this result suggests the one-neutron removal cross section to be an observable more sensitive to the projectile configuration (see Sec. IV B).

To investigate the sensitivity of our calculations to the construction of the phase-shift function, we also compute $\sigma_R(^{31}\text{Ne})$ using the OLA (5) (dotted lines in Fig. 4). As is usually observed [23,37], the OLA tends to predict larger cross sections. However, the difference between the reaction cross sections obtained with the $1p_{3/2}$ configuration and the $0f_{7/2}$ one is about the same using OLA (5) as when the phase-shift function (6) is used.

Figure 5 displays $\sigma_R(^{31}\text{Ne})$ on a ^{208}Pb target calculated with only the nuclear phase shifts. The effect of Coulomb breakup is discussed in the next subsection. As observed for the carbon target, the difference between the $1p_{3/2}$ (full line) and $0f_{7/2}$
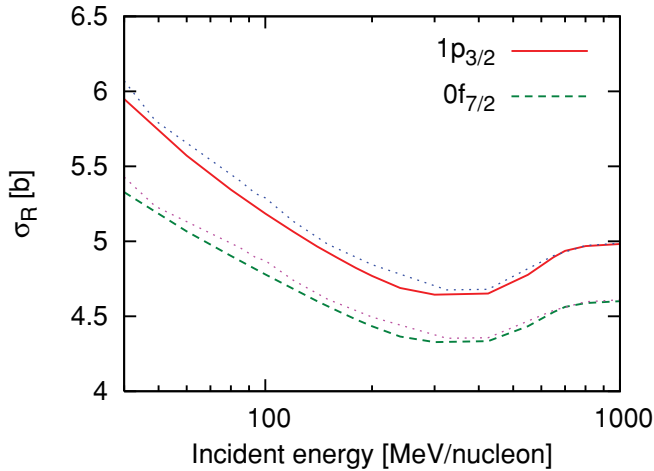
FIG. 5. (Color online) Nuclear contribution to the total reaction cross section of ^{31}Ne on a ^{208}Pb target as a function of incident energy. The dotted lines are the results obtained with the average profile functions taken from Ref. [23]. See caption of Fig. 3 for r_0 and a.

FIG. 6. (Color online) One-neutron removal cross section of ^{31}Ne, approximated by $\sigma_R(^{31}\text{Ne}) - \sigma_R(^{30}\text{Ne})$, on a ^{12}C target as a function of incident energy: $1p_{3/2}$ (range between full lines) and $0f_{7/2}$ (range between dashed lines). The experimental point is from Ref. [19].

(dashed line) configurations is small though non-negligible. As mentioned earlier, this difference comes mainly from the valence-neutron contribution. The increase of σ_R from ^{30}Ne to ^{31}Ne is even more striking for a ^{208}Pb target. It is almost 10 times larger considering a $1p_{3/2}$ valence neutron than a $0f_{7/2}$ one. At 240 MeV/nucleon, the reaction cross section increases from 4.36 b to 4.69 b in the former case while it goes from 4.33 b to only 4.37 b in the latter.

Since the proton and neutron densities of the lead target are different, we examine how much the cross sections depend on the choice of the profile function Γ_{NN}. Figure 5 compares two sets of calculations, one which employs different interactions between pp (or nn) and pn (full and dashed lines), and the other which uses the averaged interaction taken from Ref. [23] (dotted lines). As observed in Fig. 5, the choice of the averaged interaction tends to slightly overestimate the cross sections below 300 MeV/nucleon.

The enhanced cross section for the $1p_{3/2}$ orbit reflects the spatial extension of the neutron orbit. If its S_n value is increased to, say, 0.6 MeV as shown in Table II, $\sigma_R(^{31}\text{Ne})$ gets smaller compared to that with $S_n = 0.33$ MeV: At 240 MeV/nucleon, it is reduced by 12 mb for carbon and by 65 mb for lead. These cross sections are still significantly larger than those for the $0f_{7/2}$ neutron case.

B. One-neutron removal cross sections

As mentioned in Sec. II A, we evaluate the one-neutron removal cross section σ_{-n} for ^{31}Ne on carbon and lead targets using approximation (3). Figure 6 shows the results obtained on a ^{12}C target as a function of the ^{31}Ne incident energy for both $1p_{3/2}$ (full lines) and $0f_{7/2}$ (dashed lines) configurations. To evaluate the sensitivity of these results to the potential set used to generate the projectile densities, we have performed the calculations with the different potentials given in Tables I and II. Though the $1p_{3/2}$ or $0f_{7/2}$ orbits vary with the potential
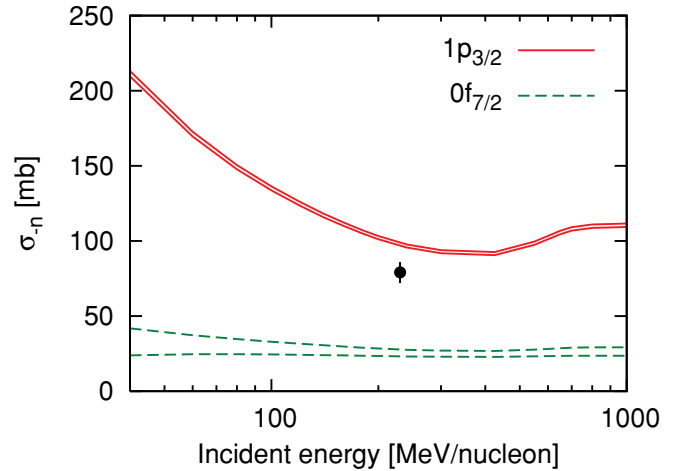
set, they predict very similar σ_{-n} values: In both cases these values are contained between the pairs of lines shown in Fig. 6. Hereafter we use the potential set with $r_0 = 1.25$ fm and $a = 0.75$ fm for the $1p_{3/2}$ orbit, and the set with $r_0 = 1.25$ fm and $a = 0.70$ fm for the $0f_{7/2}$ orbit unless otherwise mentioned.

As discussed in the previous subsection, the interesting result of this set of calculations is that σ_{-n} is always much larger for a $1p_{3/2}$ valence neutron than for a $0f_{7/2}$ one. At 240 MeV/nucleon, close to the energy of the RIKEN experiment [19], the former configuration leads to a cross section of about 96 mb, whereas the latter gives only 26 mb. This difference is basically due to the larger spatial extension of the p orbit compared to that of the f orbit, which is due to the change in the centrifugal barrier. The experimental cross section amounts to 79(7) mb [19]. This value, being both close to our $1p_{3/2}$ calculation and much higher than our $0f_{7/2}$ one, favors a ground-state wave function for ^{31}Ne strongly dominated by a configuration in which the valence neutron is in the $1p_{3/2}$ orbital coupled to a ^{30}Ne core in its 0^+ ground state. This comparison therefore suggests a $3/2^-$ spin-parity for the ^{31}Ne ground state rather than the $7/2^-$ deduced from the naive shell model.

As shown in Fig. 6, the difference in the magnitude of σ_{-n} increases at lower incident energies. An experiment performed at such an energy (e.g., a few tens of MeV/nucleon) would improve the confidence in the identification of the ^{31}Ne configuration.

To evaluate σ_{-n} for a ^{208}Pb target we may no longer neglect the Coulomb contribution to the one-neutron removal process. Since the Coulomb interaction contributes mostly to the elastic breakup, we add an estimate of the Coulomb-breakup cross section to the reaction cross section computed within the Glauber framework. To this end, we use the first-order of the perturbation theory, considering only the dominant dipole transition. In that approximation, the $1p_{3/2}$ neutron is excited to continuum states with $l = 0$ or 2, whereas the
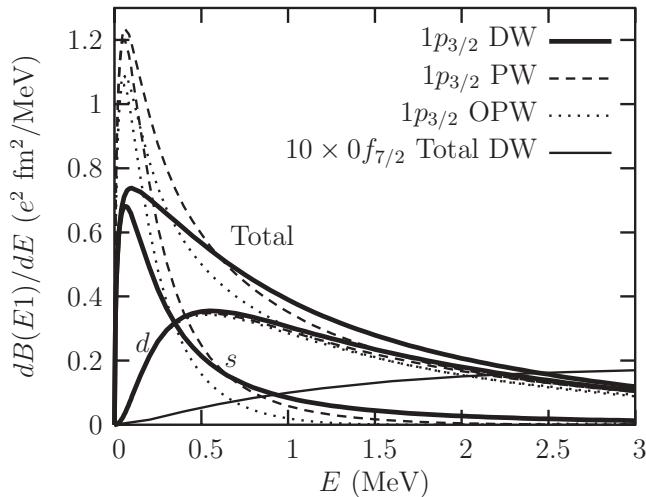
FIG. 7. Electric dipole transition strength of ^{31}Ne as a function of the c-n relative energy E after dissociation. For the $1p_{3/2}$ transition, both contributions from the s- and d-wave continuum states are shown. Results obtained with distorted waves (DW, full lines), plane waves (PW, dashed lines), and orthogonalized plane waves (OPW, dotted lines) are shown separately.

$0f_{7/2}$ neutron is moved to d or g positive-energy states. This Coulomb contribution to σ_{-n} can be estimated by integrating the electric dipole transition strength $dB(E1)/dE$ multiplied by the photon number spectrum over the excitation energy [20]. Figure 7 compares the $dB(E1)/dE$ distributions for the initial p (thick full lines) and f orbits (thin full line). In the former case, the partial-wave contributions are shown as well. Note that the result obtained from the initial $0f_{7/2}$ configuration is multiplied by 10 for readability. These quantities depend on the choice of a minimum impact parameter $b_{\min}$ from which the Coulomb breakup is assumed to contribute. However, the dependence of σ_{-n} on $b_{\min}$ is found to be moderate around $b_{\min} = 12.7$ fm, which is obtained from $b_{\min} = r_{\text{eff}}(31^{1/3} + 208^{1/3})$, with $r_{\text{eff}} = 1.4$ fm.

The dipole strength obtained for the $1p_{3/2}$ configuration is concentrated at low excitation energy. The s wave gives a larger contribution to that distribution than the d wave at $E < 0.5$ MeV, but the d wave dominates over the s wave with increasing energy. On the contrary, $dB(E1)/dE$ for the $0f_{7/2}$ initial state, besides being much smaller than the $1p_{3/2}$ one, has a completely different energy dependence: It is flat and extends to high energies. This suggests that differential observables, like energy or parallel-momentum distributions, could be used to discriminate between these two possible configurations (see Sec. V).

To evaluate the sensitivity of this calculation to the c-n final-state interactions, we evaluate the dipole strength for the initial $1p_{3/2}$ bound state using distorted waves (DW, i.e., positive-energy eigenstates of the c-n Hamiltonian (8); full lines), plane waves (PW; dashed lines), or orthogonalized plane waves (OPW, i.e., plane waves orthogonalized to the Pauli-forbidden bound states of Hamiltonian (8) [26]; dotted lines). Interestingly only the s-wave contribution is sensitive to the continuum description: That value is much reduced in the vicinity of its maximum when DW are considered instead

of PW or OPW. Nevertheless, these changes do not affect the results as much as to modify our conclusions.

At 240 MeV/nucleon, and using DW, we obtain 0.81 b for the Coulomb contribution to σ_{-n}: 0.32 b from the s wave and 0.49 b from the d waves. This value is added incoherently to the nuclear contribution to σ_{-n}, which is estimated to be about 0.33 b in the Glauber model. The resulting σ_{-n} value turns out to be 1.14 b. As expected, the dipole strength obtained for the f orbit is much smaller: Its contribution to σ_{-n} is a mere 57 mb. The nuclear contribution is evaluated in the Glauber model to be about 34 mb, leading to a total $\sigma_{-n} = 91$ mb. This is about one order of magnitude smaller than the cross section for the p orbit. The experiment performed at RIKEN gave $\sigma_{-n} = 712(65)$ mb [19]. Thus again slightly below our theoretical prediction for the $1p_{3/2}$ configuration, and much higher than the cross section obtained for the $0f_{7/2}$ orbit. This confirms the shell inversion predicted by former structure calculations [4,16], in agreement with the analysis of Nakamura *et al.* [19]. Note that evaluations of the Coulomb contribution using PW or OPW lead to similar results: large σ_{-n} for the $1p_{3/2}$ configuration and small σ_{-n} for the $0f_{7/2}$ one.

As mentioned in the last paragraph of the previous subsection, the Coulomb breakup contribution is very sensitive to S_n of the $1p_{3/2}$ orbit. We have repeated the calculation assuming $S_n = 0.6$ MeV. The σ_{-n} value for $S_n = 0.6$ MeV is predicted to be 0.75 b, of which 0.49 b is due to the Coulomb breakup. Changing S_n from 0.33 to 0.6 MeV thus reduces σ_{-n} by 0.32 b. This is much larger than the corresponding reduction (65 mb) in the nuclear breakup contribution. Since σ_{-n} changes significantly as a function of S_n mainly because of the Coulomb dissociation, a close analysis of σ_{-n} on a ^{208}Pb target can give some constraint on the S_n value of ^{31}Ne. The one-neutron removal cross section obtained with $S_n = 0.6$ MeV being closer to the experimental value suggests that the one-neutron separation energy of ^{31}Ne might be higher than 0.33 MeV. However, this reduction from theory to experiment may also be due to a spectroscopic factor for the $1p_{3/2}$ configuration smaller than 1. Other observables, like energy or parallel-momentum distributions for elastic breakup, may provide further valuable information.

V. EIKONAL CALCULATION OF ENERGY AND PARALLEL-MOMENTUM DISTRIBUTIONS

Besides the significant difference in magnitude between the one-neutron removal cross section, the distinction between the $1p_{3/2}$ and $0f_{7/2}$ configurations for ^{31}Ne could be made by looking at differential breakup observables, like energy or parallel-momentum distributions. To analyze the influence of the ^{31}Ne configuration on such cross sections, we perform elastic-breakup calculations within the Coulomb-corrected eikonal model (CCE, see Sec. II B and Ref. [27]). Unlike the Glauber model, the CCE solves the divergence problem posed by the Coulomb interaction between the projectile and the target. This enables us to take account of nuclear and Coulomb interactions on the same footing and to include their interference in the description of the reaction process. The
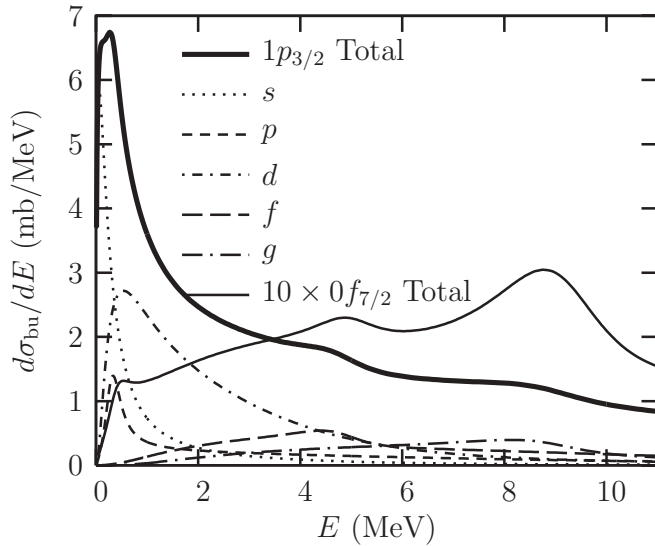
FIG. 8. Energy distribution for the elastic breakup of ^{31}Ne on carbon at 240 MeV/nucleon. The total cross section for the initial $1p_{3/2}$ bound state is plotted as well as its major partial-wave contributions. The result obtained with the initial $0f_{7/2}$ bound state, multiplied by 10, is shown for comparison.

following calculations are performed with the inputs detailed in Sec. III.

The elastic-breakup cross sections obtained for ^{31}Ne impinging on a carbon target at 240 MeV/nucleon are shown in Fig. 8 as a function of the energy E between the ^{30}Ne core and the neutron after dissociation. The total cross section for the $1p_{3/2}$ configuration is displayed with the thick full line, while its dominant s–g contributions are plotted with interrupted lines. The breakup cross section obtained considering the $0f_{7/2}$ ground state is depicted with the thin full line. Note that it is multiplied by 10 for readability. Both distributions differ significantly. First, as already mentioned in Sec. IV B, the magnitude of the $0f_{7/2}$ cross section is much lower than the $1p_{3/2}$ one. Second, the $1p_{3/2}$ distribution is strongly peaked at low energy, whereas the $0f_{7/2}$ distribution extends over a broader energy domain. This confirms that in addition to one-neutron removal cross sections, energy distributions could be used to determine the configuration of ^{31}Ne ground state.

The two bumps observed in the $0f_{7/2}$ cross section at about 5 and 9 MeV correspond to $f_{5/2}$ and $g_{9/2}$ resonances of widths $\Gamma_{0f_{5/2}} \simeq 1.5$ MeV and $\Gamma_{0g_{9/2}} \simeq 3$ MeV, respectively. These resonances are produced by the c-n potential used in this calculation (see Table II) but were not fitted to any known state. In the present work they have thus no physical meaning. However, this result indicates that if ^{31}Ne were to exhibit resonant states with a strong ^{30}Ne-n cluster structure, these could be revealed by a measurement of elastic breakup on a light target [39].

These resonances are also present in the $1p_{3/2}$ calculation, but the bumps they generate are less marked than in the $0f_{7/2}$ case. The $1p_{3/2}$ orbit, being two quanta of orbital angular momentum further away from the resonances than the $0f_{7/2}$ state, is indeed less prone to be excited toward that part of the continuum.
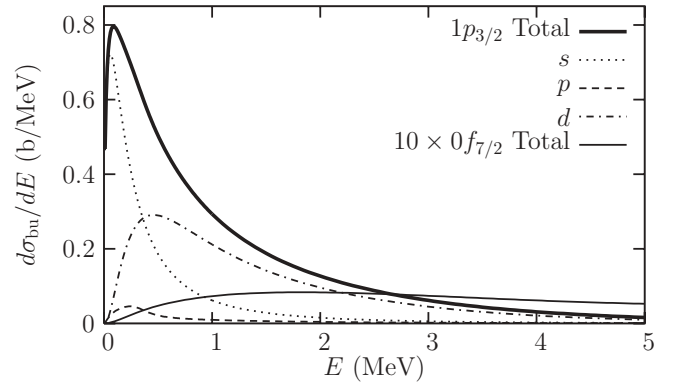

FIG. 9. Same as Fig. 8 for a lead target. Note the change in the energy axis.

We also perform a similar calculation for a ^{208}Pb target. The corresponding energy distributions are plotted in Fig. 9. As in the nuclear breakup case, the two configurations lead to very different results. Not only is the magnitude of the distribution strongly dependent on the initial state (note that the $0f_{7/2}$ cross section is multiplied by 10), but also its shape clearly reveals the configuration of ^{31}Ne ground state. As in Figs. 8 and 7, the $1p_{3/2}$ energy distribution is peaked at low energy and decreases rapidly with E. The $0f_{7/2}$ cross section, on the contrary, is much flatter.

Another observable that is often used to discriminate the orbital of valence nucleons is the parallel-momentum distribution [40–42]. In that case, the breakup cross section is evaluated as a function of the parallel momentum between the core and the neutron after dissociation. Figure 10 depicts the parallel-momentum distribution for the elastic breakup of ^{31}Ne on a carbon target at 240 MeV/nucleon. The results obtained with both the $1p_{3/2}$ (thick line) and $0f_{7/2}$ (thin line) configurations are shown. Note that here also the latter is multiplied by 10 for clarity.

The signature of the initial configuration is even clearer here than in the energy distribution. Besides the significant change in magnitude, we observe that the $0f_{7/2}$
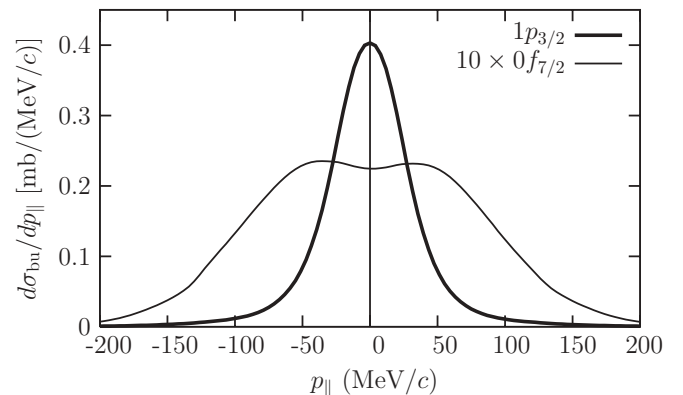

FIG. 10. Parallel-momentum distribution for the elastic breakup of ^{31}Ne on carbon at 240 MeV/nucleon. The cross section for the initial $1p_{3/2}$ bound state is compared to that obtained with the initial $0f_{7/2}$ bound state. The latter is multiplied by 10.

parallel-momentum distribution is much broader than that of the $1p_{3/2}$ configuration. This distribution can be understood as a reminiscence of the initial bound-state wave function expressed in the momentum space [40,42]. The large spatial expansion of the $1p_{3/2}$ wave function translates into a narrow momentum distribution, which is revealed in this breakup cross section. On the contrary, the narrower spatial distribution of the $0f_{7/2}$ state leads to the broader parallel-momentum distribution observed in Fig. 10.

VI. CONCLUSION AND PERSPECTIVES

The very neutron-rich isotope ^{31}Ne ($N = 21$) is located in a region where mixing of normal and intruder shell configurations is expected. In a naive shell model, the ^{31}Ne ground state would be seen as a ^{30}Ne core in its 0^+ ground state to which a $0f_{7/2}$ valence neutron is added. However, some calculations predict this valence neutron to be in a $1p_{3/2}$ intruder orbital instead [4,16]. If this were the case, the low angular momentum of the orbital combined to the low one-neutron separation energy of ^{31}Ne ($S_n \simeq 0.33$ MeV [13]) would suggest this nucleus to exhibit a one-neutron halo.

Recently, the new RIBF facility at RIKEN has produced a ^{31}Ne beam at about 230 MeV/nucleon. This beam is sufficiently intense to allow the measurement of its total reaction and one-neutron removal cross sections on carbon and lead targets [18,19]. The present work aims at analyzing the sensitivity of these cross sections to the structure of the exotic isotope ^{31}Ne. To this aim we use the Glauber model detailed in Ref. [23] to evaluate σ_R and σ_{-n}. This theoretical work shows that both σ_R and σ_{-n} computed considering a $1p_{3/2}$ configuration for ^{31}Ne are larger than those obtained with a $0f_{7/2}$ valence neutron. Especially, the difference in σ_{-n} is significant enough to doubtlessly discriminate between the two possible configurations. During the completion of this theoretical work, the one-neutron removal cross sections of ^{31}Ne measured at RIKEN became available [19]. The comparison of these data to our calculations suggests a strong $1p_{3/2}$ configuration in the wave function of ^{31}Ne ground state, confirming, independently from the analysis of Nakamura *et al.* [19], the expected shell inversion in ^{31}Ne. We therefore conclude the spin-parity of that ground state to be $3/2^-$ rather than $7/2^-$ as suggested by the naive shell model.

Since other observables could be used to test this shell inversion, we have also performed prospective calculations within the Coulomb-corrected eikonal approximation [27] for the breakup of ^{31}Ne on both carbon and lead targets. These calculations confirm that a $0f_{7/2}$ configuration would lead to much smaller breakup cross sections than if the valence neutron were in the intruder $1p_{3/2}$ orbital. They also show that the shape of the energy and parallel-momentum distributions could be used to distinguish between the two possible configurations. Indeed, whereas assuming a $1p_{3/2}$ valence neutron gives energy distributions peaked at low energy, the $0f_{7/2}$ configuration leads to distributions that reach much higher energies. We have also observed that the parallel-momentum distribution is much narrower when the bound state is assumed in the p partial wave than in the f one. The measurement of these distributions would therefore provide a complementary way to confirm the structure information obtained from the recent RIKEN measurement of σ_{-n}.

At such a distance from the valley of stability and near the region of the island of inversion, the ^{31}Ne ground state may not be composed of a single configuration. An extension of the reaction models used in this work to a multiple-configuration description of the projectile structure, as the one proposed by Summers *et al.* [43], would definitely improve the reaction model. Such a model would indeed help understanding the influence of a multiple-configuration structure of the projectile on reaction observables.

[1] H. Horiuchi and K. Ikeda, Prog. Theor. Phys. **40**, 277 (1968).

[2] Y. Fujiwara, H. Horiuchi, K. Ikeda, M. Kamimura, K. Katō, Y. Suzuki, and E. Uegaki, Prog. Theor. Phys. Suppl. **68**, 29 (1980).

[3] W. Geithner, T. Neff, G. Audi, K. Blaum, P. Delahaye, H. Feldmeier, S. George, C. Guénaut, F. Herfurth, A. Herlert *et al.*, Phys. Rev. Lett. **101**, 252502 (2008).

[4] A. Poves and J. Retamosa, Nucl. Phys. **A571**, 221 (1994).

[5] E. Caurier, F. Nowacki, A. Poves, and J. Retamosa, Phys. Rev. C **58**, 2033 (1998).

[6] Y. Utsuno, T. Otsuka, T. Mizusaki, and M. Honma, Phys. Rev. C **60**, 054315 (1999).

[7] M. Kimura and H. Horiuchi, Prog. Theor. Phys. **107**, 33 (2002).

[8] M. Kimura and H. Horiuchi, Prog. Theor. Phys. **111**, 841 (2004).

[9] Z. Dombrádi, Z. Elekes, A. Saito, N. Aoi, H. Baba, K. Demichi, Z. Fülöp, J. Gibelin, T. Gomi, H. Hasegawa *et al.*, Phys. Rev. Lett. **96**, 182501 (2006).

[10] P. Doornenbal, H. Scheit, N. Ao, S. Takeuchi, K. Li, E. Takeshita, H. Wang, H. Baba, S. Deguchi, N. Fukuda *et al.*, Phys. Rev. Lett. **103**, 032501 (2009).

[11] M. V. Stoitsov, J. Dobaczewski, W. Nazarewicz, S. Pittel, and D. J. Dean, Phys. Rev. C **68**, 054312 (2003).

[12] M. Notani, H. Sakurai, N. Aoi, Y. Yanagisawa, A. Saito, N. Imai, T. Gomi, M. Miura, S. Michimasa, H. Iwasaki *et al.*, Phys. Lett. **B542**, 49 (2002).

[13] G. Audi, A. H. Wapstra, and C. Thibault, Nucl. Phys. **A729**, 337 (2003).

[14] I. Hamamoto, S. V. Lukyanov, and X. Z. Zhang, Nucl. Phys. **A683**, 255 (2001).

[15] I. Hamamoto, Phys. Rev. C **76**, 054319 (2007).

[16] P. Descouvemont, Nucl. Phys. **A655**, 440 (1999).

[17] H. Sakurai, N. Aoi, A. Goto, M. Hirai, N. Inabe, M. Ishihara, H. Kobinata, T. Kubo, H. Kumagai, T. Nakagawa *et al.*, Phys. Rev. C **54**, R2802 (1996).

[18] T. Ohtsubo (private communication).

[19] T. Nakamura, N. Kobayashi, Y. Kondo, Y. Satou, N. Aoi, H. Baba, S. Deguchi, N. Fukuda, J. Gibelin, N. Inabe *et al.*, Phys. Rev. Lett. **103**, 262501 (2009).

[20] Y. Suzuki, R. G. Lovas, K. Yabana, and K. Varga, *Structure and Reactions of Light Exotic Nuclei* (Taylor & Francis, London, 2003).

[21] J. Al Khalili and F. M. Nunes, J. Phys. G **29**, R89 (2003).

[22] C. A. Bertulani and P. Danielewicz, *Introduction to Nuclear Reactions* (Institute of Physics Publishing, Bristol, 2004).

[23] W. Horiuchi, Y. Suzuki, B. Abu Ibrahim, and A. Kohama, Phys. Rev. C **75**, 044607 (2007).

[24] R. J. Glauber, in *Lecture in Theoretical Physics*, edited by W. E. Brittin and L. G. Dunham (Interscience, New York, 1959), Vol. 1, p. 315.

[25] J. Margueron, A. Bonaccorso, and D. M. Brink, Nucl. Phys. **A720**, 337 (2003).

[26] B. Abu Ibrahim and Y. Suzuki, Prog. Theor. Phys. **112**, 1013 (2004).

[27] P. Capel, D. Baye, and Y. Suzuki, Phys. Rev. C **78**, 054602 (2008).

[28] K. Hencken, G. Bertsch, and H. Esbensen, Phys. Rev. C **54**, 3043 (1996).

[29] C. A. Bertulani and P. G. Hansen, Phys. Rev. C **70**, 034609 (2004).

[30] D. Baye, P. Capel, and G. Goldstein, Phys. Rev. Lett. **95**, 082502 (2005).

[31] K. Yabana, Y. Ogawa, and Y. Suzuki, Nucl. Phys. **A539**, 295 (1992).

[32] Y. Ogawa, K. Yabana, and Y. Suzuki, Nucl. Phys. **A543**, 722 (1992).

[33] B. Abu Ibrahim and Y. Suzuki, Phys. Rev. C **61**, 051601(R) (2000).

[34] B. Abu Ibrahim and Y. Suzuki, Phys. Rev. C **62**, 034608 (2000).

[35] M. Abramowitz and I. A. Stegun, *Handbook of Mathematical Functions* (Dover, New York, 1970).

[36] A. Bohr and B. R. Mottelson, *Nuclear Structure* (Benjamin, New York, 1969), Vol. 1.

[37] B. Abu Ibrahim, W. Horiuchi, A. Kohama, and Y. Suzuki, Phys. Rev. C **77**, 034607 (2008).

[38] P. Capel, D. Baye, and V. S. Melezhik, Phys. Rev. C **68**, 014612 (2003).

[39] P. Capel, G. Goldstein, and D. Baye, Phys. Rev. C **70**, 064605 (2004).

[40] P. G. Hansen, Phys. Rev. Lett. **77**, 1016 (1996).

[41] E. Sauvan, F. Carstoiu, N. A. Orr, J. C. Angélique, W. N. Catford, N. M. Clarke, M. M. Cormick, N. Curtis, M. Freer, S. Grévy *et al.*, Phys. Lett. **B491**, 1 (2000).

[42] P. G. Hansen and J. A. Tostevin, Annu. Rev. Nucl. Part. Sci **53**, 219 (2003).

[43] N. C. Summers, F. M. Nunes, and I. J. Thompson, Phys. Rev. C **74**, 014606 (2006).